ISSN (Print) 1226-1750
ISSN (Online) 2233-6656
Journal of Magnetics 30(4), 746-751 (2025) https://doi.org/10.4283/JMAG.2025.30.4.746

Detector Design using Block Scintillator with 4-Sided Light Sensor and MLPE for Achieving High Resolution and High Sensitivity in Small Animal PET/MRI

Seung-Jae Lee[1,2]*

[1]*Department of Radiological Science, Dongseo University, Busan 47011, Republic of Korea*
[2]*Center for Radiological Environment & Health Science, Dongseo University, Busan 47011, Republic of Korea*

(Received 29 October 2025, Received in final form 17 December 2025, Accepted 17 December 2025)

A detector utilizing a block scintillator and a semiconductor light sensor was designed for small animal positron emission tomography/magnetic resonance imaging (PET/MRI) applications that achieves high resolution and sensitivity without signal distortion in a magnetic field. The goal was to achieve high sensitivity by using a block scintillator rather than a pixelated scintillator, and high resolution by applying a maximum likelihood position estimation (MLPE). A DETECT2000 simulation was performed to evaluate the performance of the designed detector. Gamma-ray events, where the scintillator and gamma-rays interact, were generated at 1 mm intervals in all directions within the scintillator, and signals were collected by the light sensor. A look-up table (LUT) was created based on the collected signals, and the measurement accuracy of the gamma-ray interaction location was evaluated using the LUT and MLPE. The results showed an excellent measurement accuracy of approximately 85.7% on average. It is considered that this detector can achieve excellent sensitivity and resolution when used in small animal PET/MRI.

Keywords : small animal PET/MRI, magnetic field, semiconductor light sensor, MLPE

1. Introduction

Small animal positron emission tomography/magnetic resonance imaging (PET/MRI) systems combine PET and MRI to image small animals. Because small animals have much smaller organs and systems than humans, PET systems offer superior spatial resolution compared to human systems. To achieve this superior spatial resolution, small animal PET systems utilize detectors with extremely small scintillation pixels. Early detectors used scintillation pixels with cross-sections of approximately 2 mm × 2 mm [1, 2], but later detectors with scintillation pixels measuring 1 mm × 1 mm or less were developed [3-5]. However, detectors with very small scintillation pixels exhibit lower sensitivity than those with larger pixels. To maximize the transfer of light generated by the interaction of the scintillation pixels with gamma rays to the light sensor, the scintillation pixels are covered with a reflector. As the scintillation pixel gets smaller, the area occupied by the reflector in the entire detector increases. Therefore the area of the scintillation pixel that interacts with the gamma rays decreases, which lowers the sensitivity. Fig. 1 compares the area occupied by the scintillation pixel when large and small scintillation pixels are used in a detector with the same area. Since the thickness of the reflector is constant, it can be confirmed that the area occupied by the scintillation pixel is smaller in the detector with small scintillation pixels that use a lot of

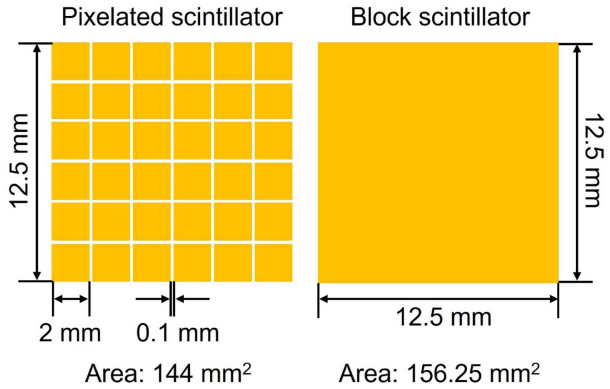

Fig. 1. (Color online) Comparison of the area occupied by the scintillator on the detector according to the size of the scintillator pixel in the same area detector.

*Corresponding author: Tel: +82-51-320-2719
e-mail: sjlee@gdsu.dongseo.ac.kr

reflectors. In previous studies, a detector using a block scintillator was designed [6, 7]. By arranging the block scintillator and the light sensors on four or six sides, a detector that can achieve high sensitivity and high resolution was designed.

In this study, a detector was designed that improves performance compared to existing designs. Using a block scintillator, light sensors are placed on each of its four sides to collect light. Based on the collected signals, the location of the gamma-ray interaction with the scintillator is measured using the maximum likelihood position estimation (MLPE) [8-10]. To evaluate the performance of the designed detector, DETECT2000 [11, 12], a light simulation tool for scintillator-based detectors, was used.

2. Materials and Methods

2.1. Detector configuration

A small animal PET/MRI detector that can achieve high resolution and sensitivity using a block scintillator was designed. High resolution was achieved by measuring the three-dimensional location of gamma-ray interactions within the block scintillator, and high sensitivity was achieved using a block scintillator rather than a pixel scintillator. Since a pixel scintillator has a reflector inserted between each pixel, the sensitivity corresponding to the reflector space is lower than that of a block scintillator. The scintillator uses a gadolinium aluminum gallium garnet (GAGG) scintillator, which has high density for detecting high-energy gamma-rays and excellent light generation for superior energy resolution [13]. GAGG generates approximately 54,000 photons per 1 MeV of gamma-ray energy, which is significantly higher than the lutetium oxyorthosilicate (LSO) scintillator (approximately 30,000 photons/MeV) [14], which is commonly used in existing PET detectors. The maximum wavelength of the generated light is approximately 530 nm. As shown in Fig. 2, the scintillator has a cubic shape with dimensions of 12.2 mm × 12.2 mm × 12.2 mm. A Hamamatsu multi-pixel photon counter (MPPC), a semiconductor sensor, was used as a light sensor to collect the light generated from the scintillator [15]. Semiconductor sensors can operate in a magnetic field without signal distortion. The MPPC consists of a 2 × 2 array of 6 mm × 6 mm pixels with a gap of 0.2 mm between pixels. The quantum efficiency of the MPPC at the maximum wavelength of the light generated from the GAGG scintillator is approximately 40%, which is superior to that of the PMT, a conventionally used light sensor [16]. The distance from the first pixel to the last pixel of the MPPC is 12.2 mm, which is the same size as the scintillator. The MPPC is

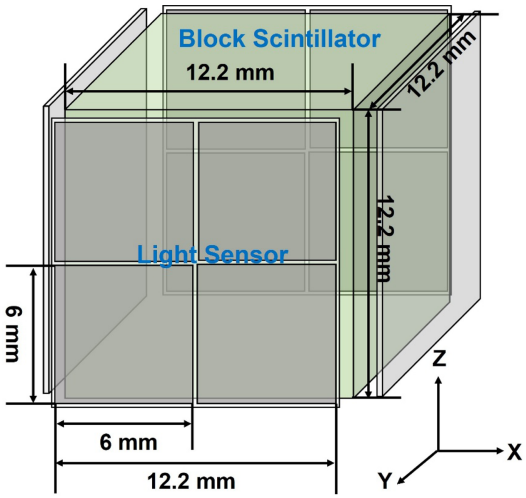

Fig. 2. (Color online) Schematic diagram of a detector designed using a block scintillator and a semiconductor photosensor.

designed to be placed on the four sides of the scintillator to collect the light generated within the scintillator. All surfaces of the scintillator, except the one coupled to the light sensor, were treated with reflective coatings. This reflective coating maximizes the light generated by the scintillator, allowing it to be collected by the light sensor, improving energy resolution. The reflector was set to a diffuse reflector with a reflectivity of 98%. Furthermore, the space between the light sensor and the scintillator was designed to eliminate air gaps using an optical grease, maximizing light transmission to the light sensor.

2.2. DETECT2000 simulation

To evaluate the performance of the designed detector, a DETECT2000 simulation was performed. Light was generated within the scintillator and collected by a light sensor. The accuracy of position measurements based on the signals generated at each location was evaluated. As shown in Fig. 3, light was generated at 1-mm intervals in all directions from a position 1.2 mm from the scintillator to 11.2 mm. One thousand gamma-ray interactions were induced at the same location. The number of generated lights was determined by considering the number of lights generated by the GAGG scintillator's interaction with annihilation radiation and the quantum efficiency of the MPPC. The light generated at each location was collected into six channels, weighted by the distance between the MPPC pixels. As shown in Fig. 4, light was collected through two channels each for the X-, Y-, and Z-axes, and a look-up table (LUT) was created using the mean and standard deviation of the light signals collected from each

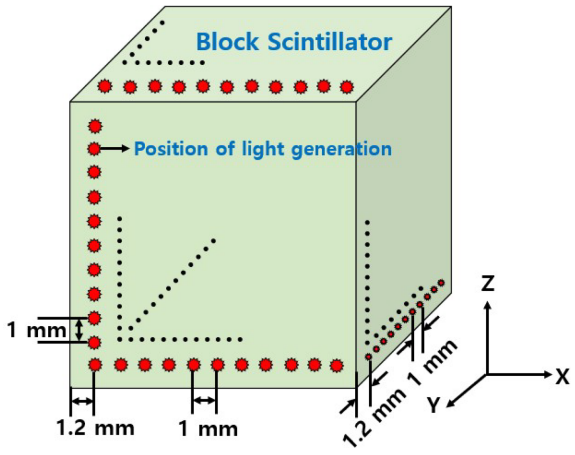

Fig. 3. (Color online) Location of light generation within the scintillator. Light was generated from the interaction between gamma rays and the scintillator at 1 mm intervals from 1.2 mm to 11.2 mm along the X, Y, and Z axes.

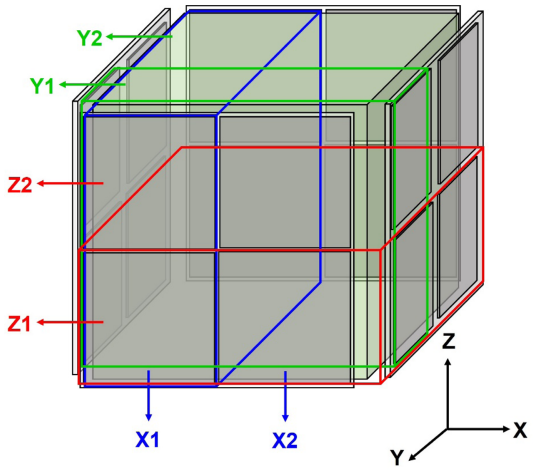

Fig. 4. (Color online) Schematic diagram of light collection for each axis for creating a lookup table. The lookup table was created by collecting light in two channels each for the X, Y, and Z axes.

channel. The accuracy of the locations where the scintillator and the gamma-ray interacted was evaluated using the created LUT and the MLPE.

3. Results

A detector was designed using a block scintillator and 2 × 2 light sensors arranged on four sides of the scintillator. Gamma-ray events were generated at 1 mm intervals in all directions from 1.2 mm to 11.2 mm within the scintillator measuring 12.2 mm × 12.2 mm × 12.2 mm. The generated light traveled within the scintillator and was ultimately collected by the light sensors arranged on the sides of the scintillator. A LUT was created based on the collected light signals. Table 1 shows a portion of the created LUT. The LUT includes the mean and standard deviation for each channel, and was created for all 11 × 11 × 11 locations. Using the created LUT, the position measurement accuracy of all locations where gamma-ray events were generated was evaluated using the MLPE. Table 2 shows the results of the position accuracy evaluation for the XYZ planes. An excellent position measurement accuracy of approximately 85.7 ± 7.2% was observed for all locations. Table 3 shows the results of the position measurement accuracy evaluation for the XY planes. The average accuracy was approximately 90.2 ± 5.2%, demonstrating superior accuracy compared to the XYZ planes. Table 4 shows the results of the position measurement accuracy evaluation for the response depth layer measurement, i.e., the Z plane. The average accuracy was approximately 90.7 ± 4.8% for all positions.

Table 1. A lookup table created by collecting light signals generated within a block scintillator. μ represents the mean, and σ represents the standard deviation.

X1 μ	X1 σ	X2 μ	X2 σ	Y1 μ	Y1 σ	Y2 μ	Y2 σ	Z1 μ	Z1 σ	Z2 μ	Z2 σ
72936.72	398.22	88038.47	418.93	72931.81	389.73	88043.39	407.87	41337.72	183.44	53596.37	198.23
75400.96	373.83	88946.00	386.33	74049.84	393.05	90297.11	389.75	42205.89	171.64	54716.67	190.47
76581.34	384.70	87843.75	398.55	74035.82	383.78	90389.27	404.95	42229.86	168.82	54738.79	193.59
77381.60	369.16	86435.06	394.95	73911.44	391.85	89905.22	410.60	42023.42	178.23	54586.40	199.33
79226.25	392.95	84888.97	392.14	74669.46	401.71	89445.75	413.23	42188.65	178.54	54597.25	191.82
81596.11	407.09	81023.86	390.04	74089.14	403.78	88530.83	409.66	41884.40	180.70	54019.69	190.29
85342.40	400.08	78755.98	385.16	74475.84	391.64	89622.54	415.16	42147.68	179.82	54628.29	187.15
86766.11	403.35	77304.72	401.44	73967.71	389.83	90103.12	390.27	42093.76	175.41	54665.96	187.69
88002.42	397.54	76412.06	394.52	74020.84	388.97	90393.65	408.13	42237.02	174.77	54725.37	189.75
89121.24	399.76	75081.16	394.75	74017.42	403.99	90184.98	395.23	42148.85	175.52	54688.46	184.42

Table 2. Position measurement accuracy results for the XYZ plane. Shows the results for each location, measured accurately along the X, Y, and Z axes.

XYZ	x1	x2	x3	x4	x5	x6	x7	x8	x9	x10	x11	average
y1	77.05	75.91	73.37	85.13	90.11	92.00	91.01	81.84	74.05	74.93	74.32	80.88
y2	76.11	77.99	79.86	83.65	83.72	84.91	85.45	81.95	78.71	78.95	74.96	80.57
y3	74.69	80.00	93.48	89.05	89.18	87.77	89.55	88.98	94.25	75.02	74.70	85.15
y4	85.48	83.55	88.45	91.65	93.59	92.35	93.22	90.72	88.27	82.03	85.65	88.63
y5	90.11	83.75	89.34	93.82	96.85	97.03	96.13	92.28	89.05	85.59	92.35	91.48
y6	91.73	84.28	88.44	92.85	96.99	96.95	96.37	91.38	88.48	85.22	93.35	91.46
y7	90.71	85.22	89.38	93.88	96.00	96.28	95.98	92.35	89.14	86.31	93.05	91.66
y8	81.49	81.17	88.60	90.45	91.79	91.43	92.55	90.19	88.90	80.59	82.77	87.27
y9	72.89	78.15	93.89	88.35	88.85	88.42	89.16	88.75	93.25	74.37	72.96	84.46
y10	74.55	78.34	74.68	80.87	84.73	84.90	86.17	81.08	73.93	78.23	75.81	79.39
y11	74.50	74.15	74.75	85.76	92.37	93.18	93.12	82.91	72.68	76.79	73.57	81.25
average	80.85	80.23	84.93	88.68	91.29	91.38	91.70	87.49	84.61	79.82	81.23	85.66

Table 3. Position measurement accuracy results for the X-Y plane. Shows the results for each location, measured accurately along the X and Y axes, excluding the positional accuracy along the Z axis.

XY	x1	x2	x3	x4	x5	x6	x7	x8	x9	x10	x11	average
y1	88.71	86.39	81.81	89.34	91.93	93.91	93.08	87.06	82.3	84.2	85.58	87.66
y2	86.48	84.3	85.77	88.15	88.22	89.47	90.11	85.94	84.67	84.46	84.77	86.58
y3	83.1	85.97	95.15	92.72	92.34	91.88	92.52	92.73	95.83	81.14	80.79	89.47
y4	89.57	88.04	92.22	96.75	96.85	95.81	96.95	95.94	91.87	85.98	88.01	92.54
y5	92.05	88.49	92.33	97.21	98.6	98.95	98.05	95.89	91.88	90.65	93.54	94.33
y6	93.87	89.02	91.95	96.05	99.05	99.07	98.54	95.38	91.98	90.15	94.37	94.49
y7	92.98	89.93	92.65	97.37	98.19	98.45	98.21	96.27	91.89	91.06	94.49	94.68
y8	86.68	85.07	92.22	96.09	95.67	95.38	96.64	95.96	92.14	84.12	85.84	91.44
y9	82.13	83.93	95.45	91.53	91.6	91.75	91.75	91.72	94.55	81.39	79.47	88.66
y10	84.34	84.47	80.4	84.73	89.93	89.93	91.16	84.57	81.2	83.66	84.55	85.36
y11	85.94	84.5	80.97	88.25	93.56	94.15	94.49	86.04	79.55	85.36	86.38	87.2
average	87.8	86.37	89.17	92.56	94.18	94.43	94.68	91.59	88.9	85.65	87.07	90.22

Table 4. Position measurement accuracy results for the Z plane. Shows the results for each location, measured accurately along the Z axis, excluding the positional accuracy along the X and Y axes.

Z	x1	x2	x3	x4	x5	x6	x7	x8	x9	x10	x11	average
y1	80.89	84.24	84.12	91.15	95.04	97.35	95.83	89.66	84.08	83.52	78.61	87.68
y2	84.37	86.87	88.25	88.55	89.65	92.65	90.05	87.78	87.74	87.17	83.41	87.86
y3	84.73	88.13	95.14	91.45	91.59	91.45	91.84	91.25	95.68	83.01	88.13	90.22
y4	91.19	88.47	91.06	92.75	94.78	94.34	94.16	92.02	90.88	87.91	94.16	91.98
y5	95.08	89.29	91.70	94.67	97.64	97.73	97.18	93.75	91.56	90.38	96.85	94.17
y6	97.17	92.39	92.08	94.51	97.69	97.56	97.37	93.27	92.35	92.77	98.66	95.08
y7	95.21	89.72	91.59	94.88	96.96	97.30	96.85	93.55	91.47	90.99	97.43	94.18
y8	89.41	87.03	91.22	91.55	93.24	93.35	93.64	91.43	91.51	87.15	92.41	91.09
y9	83.26	87.65	95.55	91.14	91.44	92.25	91.63	91.41	94.98	82.83	86.57	89.88
y10	83.27	87.14	83.05	87.48	90.18	92.77	90.86	87.07	82.36	87.23	83.93	86.85
y11	78.75	82.60	88.27	93.84	96.85	98.64	97.45	92.56	86.20	84.56	78.93	88.97
average	87.58	87.59	90.19	92.00	94.10	95.04	94.26	91.25	89.89	87.05	89.01	90.72

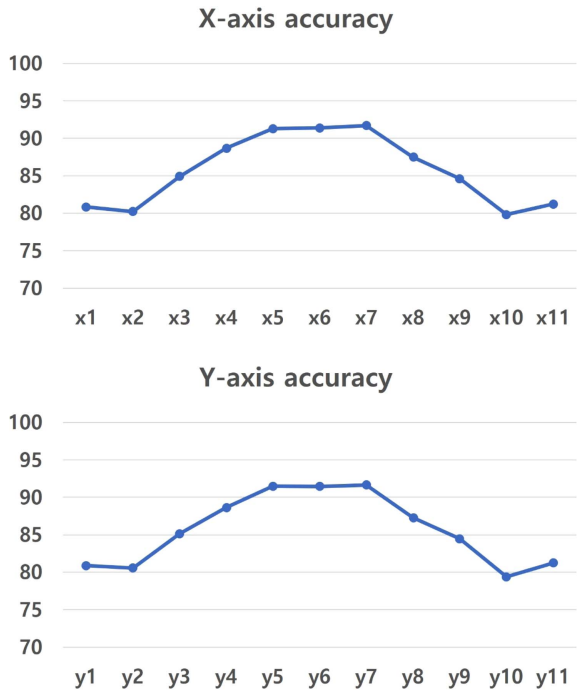

Fig. 5. (Color online) Accuracy distribution for X-axis and Y-axis positions in the XYZ plane.

The 3D position measurement had the lowest accuracy compared to the 2D and depth measurement accuracies. This is considered to be due to depth measurement errors. Fig. 5 shows the accuracy distributions for the X and Y-axis positions in the XYZ planes. For all axes, the positions were measured with low accuracy at the edges of the scintillator, while the center was measured with excellent accuracy. This is considered to be due to the minimal difference in the distribution of light generated at the edges. However, compared to the results obtained in previous studies, the position discrimination is considered to be better. In previous studies, edge locations were found to overlap, but in this study, 72.7% of the location measurements were made at the minimum (9, 11) location.

4. Discussion

A detector was designed with a block scintillator and light sensor placed on the side. Using a block scintillator instead of a pixel scintillator improved sensitivity. This was because the absence of a reflector between the scintillation pixels increased the area interacting with gamma rays compared to detectors using pixel scintillators. A LUT was created based on the signals collected from the side-mounted light sensor to achieve high resolution, and the locations of gamma-ray interaction were measured using MLPE. Gamma-ray events were generated at 1-mm intervals within the scintillator, and the accuracy of the location measurements was evaluated. All locations were measured with an excellent average accuracy of 85.7%. Although relatively low accuracy was observed at two points in the scintillator edge region, which overlapped and made them indistinguishable in previous studies, this study achieved an accuracy of over 70%, suggesting that even better spatial resolution can be achieved.

5. Conclusions

A new type of detector capable of achieving high resolution and high sensitivity was designed. When this detector is used in a PET/MRI system for small animals, it is expected that signals can be measured without signal distortion in a high magnetic field by using a semi-conductor optical sensor, high sensitivity can be achieved through a block scintillator, and high resolution can be achieved by acquiring images with a spatial resolution of less than 1 mm through the MLPE method.

Acknowledgments

This work was supported by Dongseo University 『Dongseo Frontier Project』 Research Fund of 2025.

References

[1] S. R. Cherry, Y. Shao, R. W. Silverman, K. Meadors, S. Siegel, A. Chatziioannou, J. W. Young, W. Jones, J. C. Moyers, D. Newport, A. Boutefnouchet, T. H. Farquhar, M. Andreaco, M. J. Paulus, D. M. Binkley, R. Nutt, and M. E. Phelps, IEEE Trans. Nucl. Sci. **44**, 1161 (1997).
[2] C. Knoess, S. Siegel, A. Smith, D. Newport, N. Richer-zhagen, A. Winkeler, A. Jacobs, R. N. Goble, R. Graf, K. Wienhard, and W.-D. Heiss, Eur. J. Nucl. Med. Mol. Imaging **30**, 737 (2003).
[3] S. Yamamoto, H. Watabe, T. Watabe, H. Ikeda, Y. Kanai, Y. Ogata, K. Kato, and J. Hatazawa, Nucl. Instrum. Methods Phys. Res. A **836**, 7 (2016).
[4] Y. Yang, J. Bec, J. Zhou, M. Zhang, M. S. Judenhofer, X. Bai, K. Di, Y. Wu, M. Rodriguez, P. Dokhale, K. S. Shah, R. Farrell, J. Qi, and S. R. Cherry, J. Nucl. Med. **57**, 1130 (2016).
[5] F. Godinez, K. Gong, J. Zhou, M. S. Judenhofer, A. J. Chaudhari, and R. D. Badawi, IEEE Trans. Radiat. Plasma Med. Sci. **2**, 7 (2018).
[6] S. J. An and S.-J. Lee, J. Korean Soc. Radiol. **18**, 749 (2024).
[7] W. Jo, S-J. Lee, and C-H. Baek, New Phys.: Sae Mulli. **75**, 818 (2025).

[8] H. H. Barrett, W. C. J. Hunter, B. W. Miller, S. K. Moore, Y. Chen, and L. R. Furenlid, IEEE Tran. Nucl. Sci. **56**, 725 (2009).
[9] S.-J. Lee, B. Jo, and S.-Y. Cho, J. Magn. **28**, 409 (2023).
[10] S.-J. Lee and C-H. Baek, J. Magn. **30**, 448 (2025).
[11] F. Cayouette, D. Laurendeau, and C. Moisan, Proc. SPIE, Quebec **4833**, 69 (2003).
[12] F. Cayouette, C. Moisan, N. Zhang, and C. J. Thompson, IEEE Trans. Nucl. Sci. **49**, 624 (2002).
[13] GAGG scintillator, https://www.epic-crystal.com/scintillation-crystals/gaggce-crystal.html
[14] LSO scintillator, https://www.epic-crystal.com/scintillation-crystals/lysoce-crystal.html
[15] Hamamatsu MPPC, https://www.hamamatsu.com/content/dam/hamamatsu-photonics/sites/documents/99_SALES_LIBRARY/ssd/s14160_s14161_series_kapd1064e.pdf
[16] Hamamatsu PMT, https://www.hamamatsu.com/content/dam/hamamatsu-photonics/sites/documents/99_SALES_LIBRARY/etd/R1924A_P-700_TP-MH1387E.pdf